A Simple Model for Tropical Convective Cloud Shield Area Time Tendencies Informed by Geostationary IR, GPM, and Aqua/AIRS Satellite Data

Gregory S. Elsaesser[1,2], Rémy Roca[3], Thomas Fiolleau[3],
Anthony D. Del Genio[2,†], Jingbo Wu[1,2]

[1]*Department of Applied Physics and Mathematics, Columbia University, New York, New York, USA*

[2]*NASA Goddard Institute for Space Studies, 2880 Broadway, New York, New York, USA*

[2]*Laboratoire d'Etudes en Géophysique et Océanographie Spatiales, Observatoire Midi-Pyrénées, Toulouse, France*

Corresponding Author: Gregory S. Elsaesser, Department of Applied Physics and Applied Mathematics, Columbia University/NASA Goddard Institute for Space Studies, 2880 Broadway, New York, New York, Tel: (212) 678-5596, gregory.elsaesser@columbia.edu

†*Now retired*

Key Points:

- Compositing masks much variability in convective cloud area lifecycles, thus motivating analysis of instantaneous growth and decay rates.
- A simple analytical model for cloud area growth and decay rates is developed, with a source term driven by convective cell diabatic heating.
- The model works equally well for convective systems of varying duration and degrees of convective organization over both land and ocean.

Abstract

Deep convective system maximum areal extent is driven by the stratiform anvil area since system convective area fractions are much less than unity when systems reach peak size. It is important to understand the processes that drive system size given the impact large systems have on rainfall and since anvils may strongly impact high cloud feedbacks. Using satellite diabatic heating and convective-stratiform information mapped to convective systems, composite analyses suggest that system maximum sizes occur at the temporal mid-point of system lifecycles with both maximum size and duration correlating with peak heating above the melting level. However, variations in system growth rates exist, with the overall smooth composites emerging as the average of highly variable system trajectories. Thus, this study focuses on understanding convective system growth rates on short (30-minute) timescales via development of a simple analytical source – sink model that predicts system area changes. Growth occurs when detrained convective mass (inferred from the vertical gradient of diabatic heating and temperature lapse rates) and/or generation of convective area exceeds a sink term whose magnitude is proportional to the current cloud shield size. The model works well for systems over land and ocean, and for systems characterized by varying degrees of convective organization and duration (1.5–35 hr, with correlations often >0.8 across lifetime bins). The model may serve as a useful foundation for improved understanding of processes driving changes in tropics-wide convective system cloud shields, and further supports conceptual development and evaluation of prognostic climate model stratiform anvil area parameterizations.

1 Introduction

Mesoscale convective systems (MCSs) are the dominant sources of rainfall in the tropics (Tao and Moncrieff, 2009; Roca et al., 2014; Moncrieff, 2019). MCS cloud shields comprise convective regions whose spatial aggregation may be quantified via "organization metrics" (Parker and Johnson, 2000; Tobin et al., 2012; Tobin et al., 2013; Holloway et al., 2017; Retsch et al., 2020) such that increased organization may be associated with larger cloud shields, longer lifetimes and substantial rainfall accumulation (Liu et al., 2008; Liu, 2011; Roca and Fiolleau, 2020; Schiro et al., 2020). High resolution model simulations over domains populated by MCSs are frequent sources for deriving MCS radiation, cloud, and rainfall lifecycle evolutions (Hagos et al., 2013; Feng et al., 2018; Feng et al., 2020). By mapping orbital-level satellite-estimated radiation, cloud, rainfall, and environment characteristics to the lifecycle stages of IR-tracked MCSs (as in Machado et al., 1998; Machado and Laurent, 2004; Futyan and Del Genio, 2007; Feng et al., 2012; Fiolleau and Roca, 2013b; Bouniol et al., 2016; Vant-Hull et al., 2016; Roca et al., 2017; Roca et al., 2020), or by mapping in situ environmental data to scanning radar-identified MCSs (e.g., Wang et al., 2019; Wang et al., 2020), observational composite MCS evolutions can be derived. One such compositing analysis has revealed that MCSs over the open ocean cool the sea surface temperature (SST), a signature that lasts for days (Duncan et al., 2014) and is likely to affect the subsequent development of convection.

MCS convective regions are characterized by diabatic heating profiles whose magnitudes are positive throughout most of the atmospheric column, though spread over a smaller area, while the extensive moderately raining stratiform anvil region is characterized by widespread positive heating that peaks above the melting level with diabatic cooling below (Elsaesser et al., 2010; Liu et al., 2015; Feng et al., 2018) attributed to melting snow and precipitation evaporation below cloud base. The heating profiles combine to yield top-heavy system-average heating profiles (Houze, 1989; Houze, 2004; Elsaesser et al., 2010; Hannah et al., 2016; Feng et al., 2018) that tightly couple to large-scale tropical circulations (Hartmann et al., 1984; Schumacher et al., 2004; Inoue and Back, 2015). Ice particles, laterally detrained by convection, contribute to the growth of the raining stratiform anvil region. How quickly detrained ice particles sediment impact the areal extent of the stratiform area. General circulation models (GCMs) are typically crude in their parameterization of detrained ice (Elsaesser et al., 2017; Lin et al., 2021), and thus, have trouble simulating the growth of stratiform area, let alone parameterizing MCSs (Moncrieff et al., 2017; Moncrieff, 2019). However, GCMs may still simulate relatively unbiased global rainfall and diabatic heating climatologies in the absence of successful MCS simulation, given that GCM tuning procedures focus on improving mean states (Mauritsen et al., 2012; Schmidt et al., 2017) with little or no penalty for discrepancies cancelling at the cloud-system scale. Structural parameterization errors are rarely tuned away, and they manifest themselves in biased regional rainfall rate distributions, large-scale modes of tropical variability, and cloud feedbacks. Accurate simulation of cloud feedbacks is important, and since tropical high cloud fields are largely the product of convective detrainment (Bony et al., 2016; Seeley et al., 2019) and residual MCS cloud shields, the contribution of tropical high clouds to total cloud feedbacks may be quite related to how well MCSs are simulated in the parent GCM. These complicated modes of convection are certainly one reason moist convection is a large source of uncertainty in our ability to project climate change (e.g., Bony et al., 2015; Schneider et al., 2017). Improved projections of regional rainfall distributions, more accurate simulation of cloud feedbacks and equilibrium climate sensitivity, and improved understanding of MCS trends emerging from high resolution simulations (Prein et al., 2017) and observations (Tan et al., 2015) requires continued work on determining the dominant drivers of system evolutions and their extensive cloud shields.

To this end, we perform new MCS observational analyses that build on previous MCS lifecycle compositing studies (section 3.1) and then turn our attention to the often-variable MCS cloud shield growth and decay rates, with a goal of understanding how these growth and decay rates relate to diabatic heating profiles (section 3.2 and 3.3). Since the vertical derivative of diabatic heating in convection ties to mass divergence, and mass divergence influences cloud shield changes, we contribute to research aiming to determine the factors that drive changes in stratiform anvils (e.g., Seeley et al., 2019; Hagos et al., 2020) with a focus on the development of a simple analytical source-sink model for cloud shield area changes informed by satellite data aggregated over the global tropics. These analyses will serve as a conceptual framework for continued development of organized convection parameterization in the GISS model, and can inform GCM convective parameterization development more broadly.

2 Data Sources

2.1 Satellite Observational Products

Aqua AIRS/AMSU (Chahine et al., 2006) version 6 data for temperature (available for the entire tropospheric column) and water vapor (for pressure levels > 300 hPa), along with Microwave Limb Sounder (MLS; Waters et al., 2006) version 3 data for water vapor profiles at pressure levels < 300 hPa, serve as the observed thermodynamic data sources in this work. Convective and stratiform pixel identification (Level 2 data) derived from the Global Precipitation Measurement (GPM; Skofronick-Jackson et al., 2017) mission Dual-frequency Precipitation Radar (DPR; Iguchi et al., 2012) product, rainfall from the Level 2 combined (DPR+GMI; Grecu et al., 2016) product, and diabatic heating (often denoted as Q_1-Q_R hereafter, or a heating term that includes all components except horizontal eddy flux convergence and radiative heating) from the Level 2 Convective-Stratiform Heating (CSH; Lang and Tao, 2018) and Spectral Latent Heating (SLH; Shige et al., 2009) products serve as the observed convective and stratiform precipitation and heating sources. AIRS/MLS and GPM orbital-level data are mapped to the MCS cloud shield provided by the TOOCAN convective system tracking algorithm (Fiolleau and Roca, 2013a,b). For compositing results shown in section 3, at least 1/3 of the system cloud shield must be sampled by GPM in order for measurements to be included in averaging. In order for GPM overpass data to be used in the analytical model development and associated coefficient estimation, at least 2/3 of the cloud shield must be sampled by GPM. Sensitivity of some results to this coverage threshold is discussed in section 3.4.

2.2 TOOCAN Convective System Tracking Database

The Tracking Of Organized Convection Algorithm through a 3-D segmentatioN (TOOCAN; Fiolleau and Roca, 2013a) methodology, applied to infrared (IR) data observed from a fleet of geostationary platforms, provide the MCSs used in this analysis. The TOOCAN approach aims to retain the spatial association between the convective region of MCSs and their attendant stratiform anvil component. The algorithm operates within a space-time volume of IR images, and applies a 3-D image processing technique to decompose the cold cloud shield (delineated by a 235K threshold) in the spatio-temporal domain into component MCSs. The TOOCAN algorithm is unique in that it avoids the convective system split and merge artifacts associated with traditional tracking algorithms, thus enabling MCSs and their attendant cloud shield sizes to be accurately tracked along their entire life cycles from early initiation stages to the later dissipation stages.

For this study, IR from MSG-3, GOES-13 and 15, METEOSAT-7, and MTSAT-2 are used, and MCSs within the tropical belt (30°S-30°N) from Mar – Dec 2014 are tracked. The IR sensors hosted on geostationary platforms exhibit instrument and engineering differences (e.g., different spatial and temporal resolutions, observation frequencies, spectral responses, calibrations). All IR data have been remapped to a common 0.04° equal angle grid while the temporal resolution has been unified to 30 minutes across all geostationary platforms to avoid an over-segmentation of the MCSs detected (Fiolleau et al., 2020). Additionally, there has been an effort to inter-calibrate IR data across sensors prior to ingestion into TOOCAN. The scanning schedule of MTSAT-2 does not provide a half-hourly sampling of the Southern Hemisphere region at the time of this analysis; therefore, this region is not considered in this study. Additionally, we only analyze convective systems *if* they are separated from tropical cyclones, mid-latitude cyclones, and fronts. The IBTrACS database (Knapp et al., 2010) and mid-latitude system databases (Naud et al., 2010; Naud et al., 2016) serve as the sources for selecting which MCSs to remove, with roughly 40,000 GPM-intersected systems remaining for analyses.

3 Results

3.1 Composite Convective System Diabatic Heating Lifecycles and System Durations

Several snapshots of convective systems are shown in Fig. 1. These examples suggest system sizes are predominantly driven by changing stratiform areal extent, and to a much lesser extent, varying convective extent. Close visual inspection of Fig. 1 shows that convective areas may be clustered on the edges of system shields or dispersed throughout, similar to Yuter and Houze (1998) and Fridlind et al. (2012), while anvil cloud shields extend beyond raining stratiform regions. For systems of varying durations, Fig. 2 shows the composite Q_1-Q_R, convective fractions and system sizes as a function of system lifecycle stage. Most convective systems are irregularly shaped, and the "system size" computed (and often referred to hereafter) is the diameter of a circle whose area is equivalent to the TOOCAN-identified cloud shield area. At and shortly after initiation (i.e., hr-0 lifestage), convective fractions and system sizes are similar regardless of system duration, with SLH Q_1-Q_R being of comparable magnitude for all system durations, while CSH Q_1-Q_R is surprisingly weaker in longer-lived vs shorter-lived systems. At least according to the SLH depiction, these results do not suggest a strong correspondence between early-stage convective structures and system longevity. Might the similarity in early-stage convection imply that early-stage environments are similar?

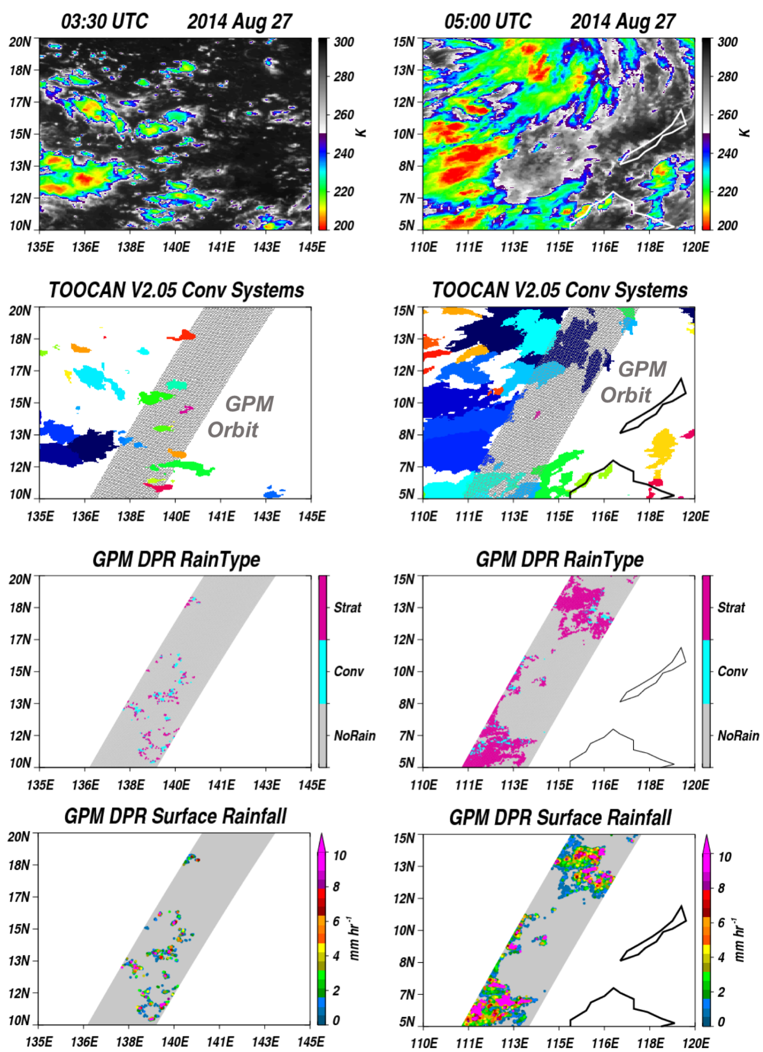

Figure 1. (Left) From top to bottom, a snapshot (03:30 UTC, 2014 Aug 27) of IR brightness temperatures, observed convective systems (distinct systems are color-coded), GPM DPR rain classification (stratiform, convective, no-surface-rain) , and GPM DPR surface rainfall. (Right) as to the left, but for a different geographic location and time (05:00 UTC).

Maturity is defined as the time at which a system reaches maximum size. At maturity, aside from longer-lived systems achieving a larger-size (a clear signature in the system size PDFs), longer-lived systems are characterized by increased maximum Q_1-Q_R (typically near 7-km) in a composite sense, with the 1σ range in peak heating for each system duration suggesting this is a robust result. Secondly, maturity marks the onset of near negligible Q_1-Q_R heating that begins in the boundary layer but gradually extends vertically to the melting level (~5-km) as the system ages and dissipates. Since convective fractions reach their minimum before maturity and are nearly invariant thereafter, this implies that system vertical heating structures and convective-stratiform fractions do not uniquely map to each other. Furthermore, it is very clear that convective-stratiform fractions do not map uniquely to duration, either.

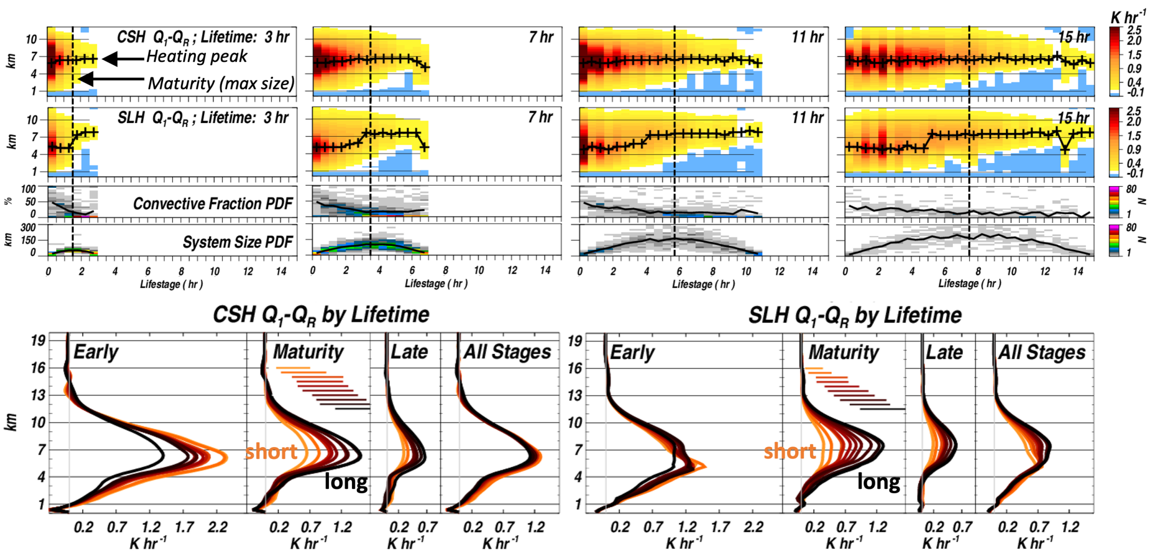

Figure 2. For convective systems of different durations (3-, 7-, 11- and 15-hr), the composite CSH and SLH Q_1-Q_R, convective fractions, and system sizes (distributions are shown for the latter two variables to illustrate variability; solid lines denote average) as a function of system lifestage. (bottom) Color coded according to system duration (3-, 5-, 7-, 9-, 11-, 13-, 15-, 19-, 25-, and 31-hr), the composite CSH and SLH Q_1-Q_R averaged over the early (initiation – 0.45), mature (0.45 – 0.55) and late (0.55 – termination) stages of the system lifecycles. For the mature-stage panel, horizontal lines denote the 1σ range in Q_1-Q_R at 7 km (color coded by duration).

Fig. 3 shows Q_1-Q_R averaged over the convective and stratiform portions of the cloud shield (in addition to system-average Q_1-Q_R composites in the top rows, as in Fig. 2). Fig. 3 suggests that CSH convective Q_1-Q_R is larger over land than ocean, consistent with studies documenting that convection over land is more intense (e.g., Zipser and Lemone, 1980; Lucas et al., 1994; Takahashi et al., 2017; Takahashi et al., 2021). SLH shows the opposite behavior in convective Q_1-Q_R, while both products yield similar stratiform heating composites. Results somewhat imply that land-ocean differences in convection from the perspective of Q_1-Q_R, convective fractions and sizes might largely arise from differences in the *occurrence frequencies* of convective system durations as opposed to distinguishable differences in a system itself characterized by the same duration. Fig. 3 further suggests that the amplitude of the stratiform heating-cooling couplet is approximately in phase with the maximum in convective heating (visually compare convective to stratiform Q_1-Q_R). Since convective heating begins rapidly dissipating shortly before maturity, the weaker convective heating in the lower troposphere is eventually overwhelmed by the overall-weaker (but somewhat lifestage-independent) stratiform anvil cooling signature which results in system-average cooling below the melting level later in the convective lifecycle (Fig. 2). Despite the stratiform heating not varying substantially as a given system progresses, it varies from one system duration to another, with longer-lived systems exhibiting larger amplitude stratiform heating-cooling signatures.

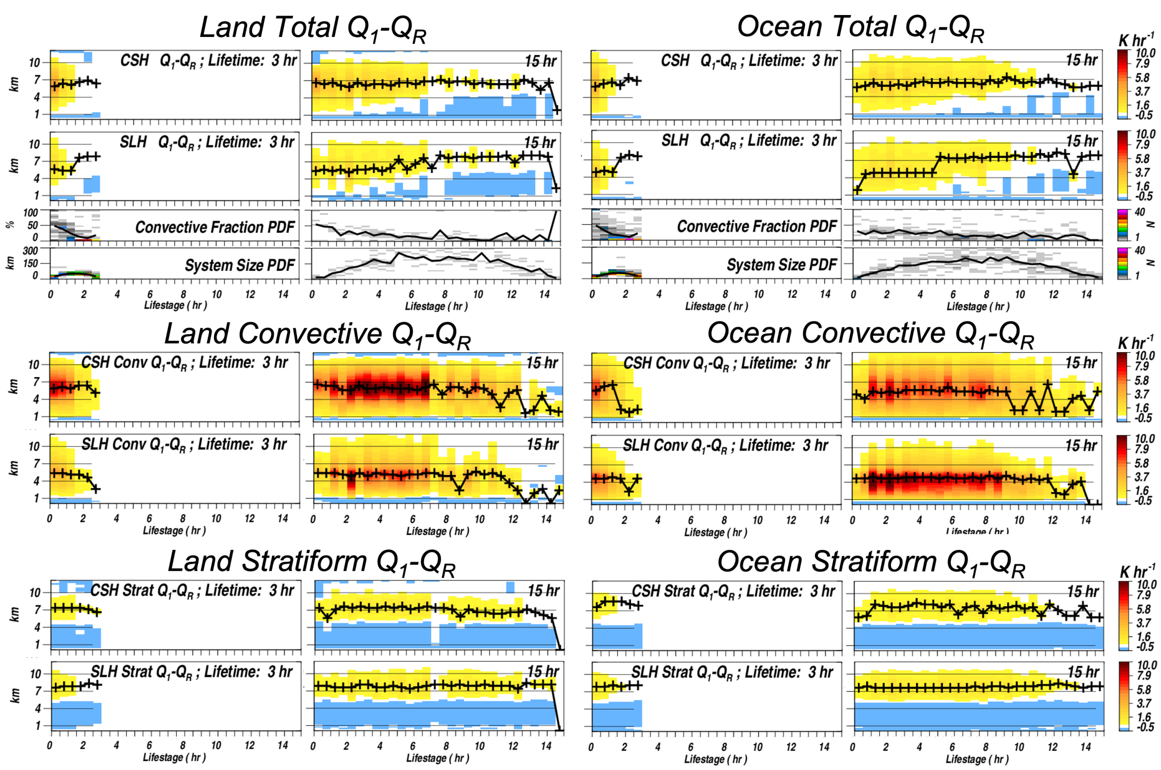

Figure 3. For convective systems of 3 and 15-hr duration (over land and ocean separately), the CSH and SLH Q_1-Q_R, convective fractions, and system sizes (distributions are shown for the latter two variables; solid lines denote average) as a function of system lifestage. Composites are also partitioned into convective region-average and stratiform region-average Q_1-Q_R components. As in Fig. 2, the plus symbols in each panel denote the altitude of peak heating as a function of lifestage. *Note the difference in magnitude range and color scales for each Q_1-Q_R panel relative to Fig. 2.*

Short- and long-lived duration systems appear to evolve similarly, and with convective fractions and heating profiles being similar at initiation, the first-order difference between a short- and long-lived duration system is the time scale for growth and decay of the convective profile and convective area (which in the composite sense, peaks consistently at a lifecycle fraction of ~0.25 for all systems). As mentioned, the stratiform heating is in phase with convective heating, but since the cloud shield size maximizes at a lifecycle fraction of 0.5 (by definition) and is largely comprised by raining stratiform area, this implies the peak in stratiform heating precedes the peak in stratiform area by roughly 0.25 multiplied by the system duration (in hours), a number that can also be inferred from Feng et al. (2012). Are these features consistent, smoothly-varying characteristics for all convective systems?

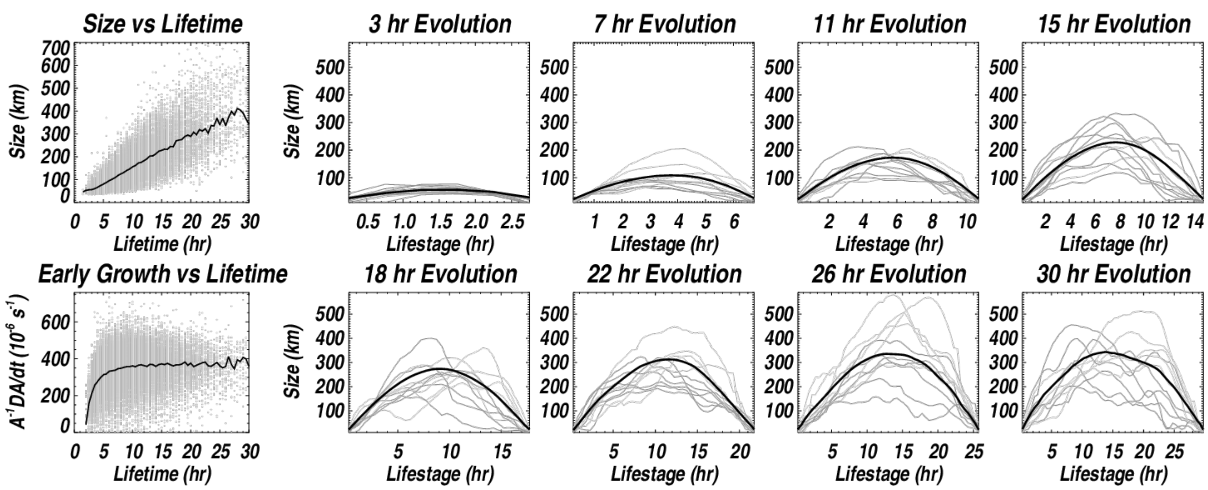

Figure 4. (top left) Convective system maximum size as a function of lifetime, with the composite relationship overplotted as a solid line; (bottom left) Early growth rate scatterplot (and solid line composite) as a function of lifetime. The remaining 8 panels show the composite system size evolution as a function of time for convective systems of varying lifetimes (solid black), with a random selection of 10 individual system evolutions overplotted for each lifetime panel (thin grey lines).

Focusing on the middle lifecycle stages of all-duration convection systems, one interpretation of the system size PDF variability of Figs. 2 and 3 is that systems hobble along, growing and decaying randomly, with the time of maximum system size deviating from the temporal mid-point but with system longevity mapping strongly to maximum size. Quantitatively, this would be reflected in a smaller correlation between individual system size temporal evolutions and the composite system size evolutions shown in Figs. 2 and 3. An alternate interpretation is that there is simply variability in the maximum system size for a system of a given lifetime (with the maximum occurring at the temporal mid-point), but with consistent increases in system size from initiation up to that point, and consistent decay toward termination, thus implying high correlation between the composite evolution and individual system evolutions. Fig. 4 sheds light on these questions. There is a clear relationship between system size and lifetime (quantitatively, the percent variance explained between maximum area and lifetime is > 50%), similar to Feng et al. (2012) and shown in Roca et al. (2017). There is, however, little relationship between growth at the early stages of convection and lifetime across durations (also similar to Feng et al., 2012), somewhat in contrast to Machado and Laurent (2004), though that study was limited to one regime and mostly focused on shorter-lived system relationships. This suggests that there is variability in the system size temporal evolution. A comparison of composite system evolutions and randomly-selected individual systems show that systems take different evolution trajectories. While many systems reach their maximum at the temporal middle point of their lifecycle (as in Roca et al. (2017) and Feng et al. (2019)), the evolutions shown here suggest that some may grow slowly, then more quickly, or vice versa.

How should we understand the system trajectories? Regardless of whether cloud shield sizes systematically increase toward a maximum and decrease after, or whether the path toward and beyond a maximum is characterized by many ups and downs, both trajectories suggest substantial variability in actual cloud shield growth rates. Considering this, and based on the results thus far, we propose to consider individual system trajectories as an accumulation of substantially varying instantaneous growth and decay sequences tied to local environments, with the overall smooth composite emerging as the average of all individual trajectories.

3.2 Convective System Cloud Shield Growth Rates and Development of Source – Sink Model

Fig. 5 shows MCS characteristics as a function of system growth and decay rates. Cloud shield size time tendency bin widths are objectively chosen so that approximately the same number of samples occur within each bin (symmetric about zero). It is clear that an asymmetry in growth and decay rates exists in top left panel of Fig. 5 with the largest growth rate magnitudes exceeding the largest decay rate magnitudes. Because decay rates on average are much slower, a short-lived sequence of rapid growth has a large potential to extend the duration of a system cloud shield area. While difficult to infer from the composite lifecycle perspectives, Fig. 5 suggests that growth in convective systems is strongly proportional to the size of the convective area and convective area Q_1-Q_R (or the vertical derivative of Q_1-Q_R above the melting level, since Q_1-Q_R tends toward zero above 15 km). For simplicity, only CSH Q_1-Q_R is shown here; a repeat of analyses using the SLH product yields similar interpretations. Is the state of convective cores themselves (Q_1-Q_R structure, and size) during growth the dominant factor in growth rates and ultimately, duration? The in-phase relationship between convective and stratiform Q_1-Q_R is much clearer from this growth – decay perspective. Growth and decay broadly map to the first and last half of the lifecycles, respectively, but, consistent with the individual system evolutions in Fig. 4, there is no one-to-one correspondence with lifecycle stage.

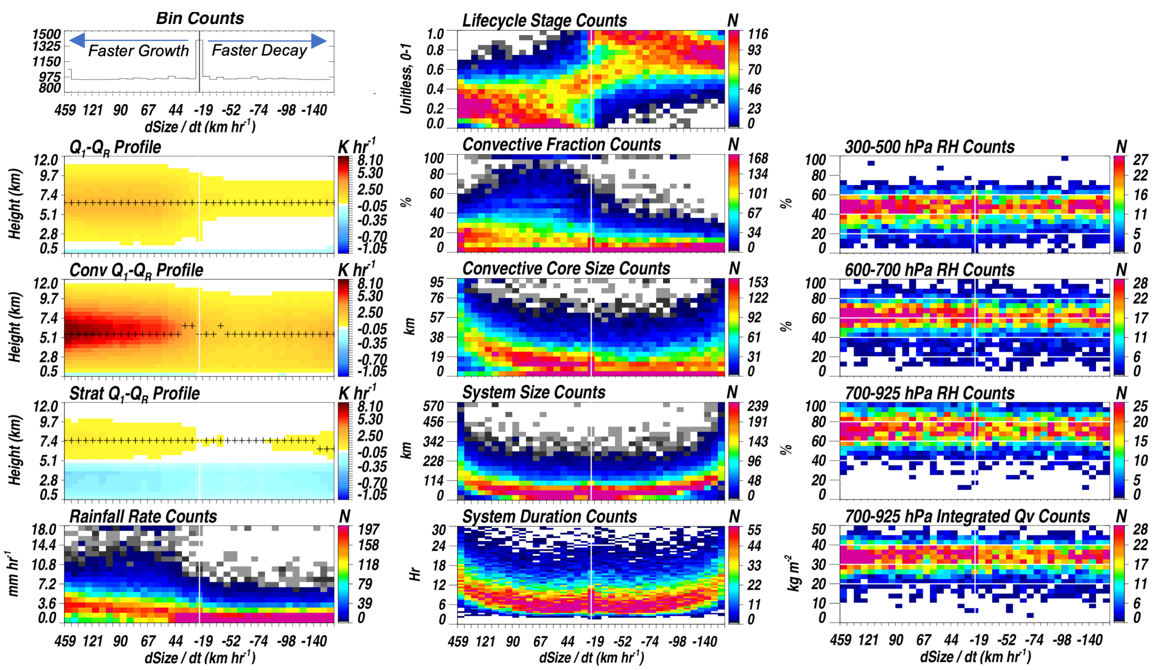

Figure 5. (left column) From top to bottom, bin counts, composite total, CSH convective and stratiform Q_1-Q_R profiles and surface rainfall rate histograms as a function of the cloud shield size rate of change. Total heating is averaged over the raining region, and convective and stratiform heating profiles are averaged over their respective cloud type areas as in Fig. 3. (middle column) Various parameter histograms plotted as a function of the cloud shield size rate of change. (right column) As in the center column, but for Aqua/AIRS retrieved relative humidity (RH) for three different levels, and integrated water vapor in the lower troposphere. As in Fig. 2, the plus symbols in the heating panels denote the altitude of peak heating. The white vertical lines denote the zero cloud shield size rate of change bin, and horizontal white lines in right column are added to aid in visual interpretation.

Nearly all of the heaviest rainfall rates are found during system growth stages. Since average rainfall peaks early in lifecycle composites (Fiolleau and Roca, 2013b; Feng et al., 2019; Feng et al., 2020) and longer-lived systems contribute more to extreme precipitation (Feng et al., 2018; Roca and Fiolleau, 2020), it is likely that the rainfall extremes specifically occur during growth periods of the early lifecycle stages. More subtle is a relationship between growth, decay, lifecycle stage, and moisture. PDFs of heating, sizes and durations, if sorted according to the RH at any level, show little variation, so the interpretation is consistent. It is worth noting that all of these RH values are much wetter than the tropics-wide average, implying that the existence of tropical MCSs depends on humid conditions, though the moisture results are consistent with the weak role that saturation fraction plays in driving rainfall duration cycles (as also shown in Elsaesser et al., 2013).

What is the cause of system cloud shield decay? It is less surprising that no relationship between growth and moisture exists, particularly if cold pool – local environment interactions (e.g., storm relative shear), gravity waves, sea breezes, or other small-scale factors are drivers of upscale growth, though some studies suggest a moistening driven by previous convection (Rapp et al., 2009; Mapes and Neale, 2011) may favor subsequent convection (which, in a Lagrangian tracking sense, implies future growth and longer duration). For the decay portion of the spectrum, when convection is absent or weak, if systems are not running into a drier environment, how do we determine why systems decay? Fig. 5 does clearly suggest that convective area is minimal during decay, and that decay rates are proportional to system size.

There is an advantage to understanding system duration from the perspective of an accumulation of growth and decay rates: if growth is related to the vertical derivative of convective Q_1-Q_R, then we can apply the concept of vertical convective mass flux convergence as a source for cloud shield area time tendencies (and thus, the magnitudes of growth rates), terms quantifiable using data from the current combination of satellite sensors in orbit. Fig. 6 shows two cases of rapidly growing cloud shields (top two rows) in systems characterized by strongly-heating convective regions and a third system, characterized by weaker convective Q_1-Q_R, whose shield is growing more slowly. The bottom two rows of Fig. 6 are examples of systems whose cloud shields are decaying. The decaying systems have little convection observed by GPM, and there is a sense that shield decay is slow and somewhat diffuse. These examples reflect the statistics shown in Fig. 5: growth can be rapid, and is likely associated with convection and a large vertical derivative of convective Q_1-Q_R.

Decay is slower and occurs with a weakened convection area, or in many cases, occurs in the absence of a convective source, while being proportional to system size.

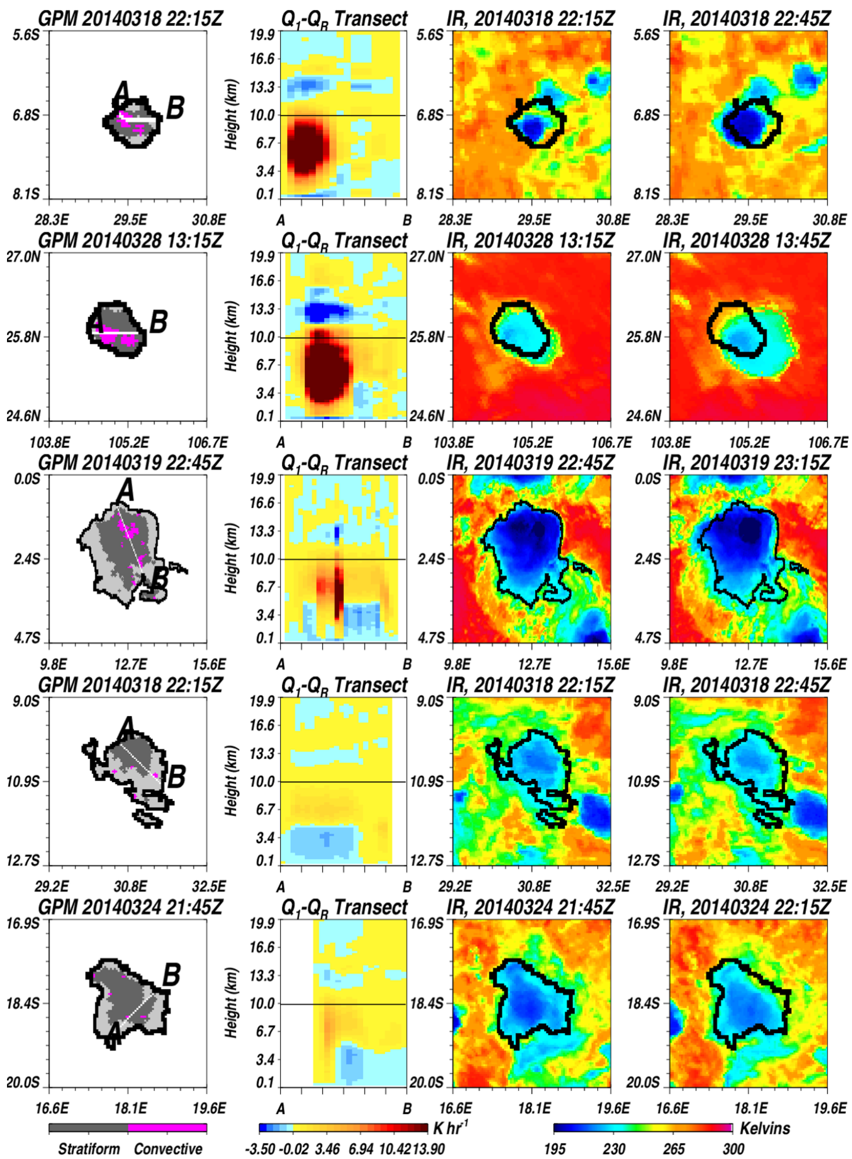

Figure 6. For different convective system examples (rows), from left to right: co-located GPM convective-stratiform field (non-raining scene shaded in light grey); CSH Q_1-Q_R profiles along the A – B transect; IR brightness temperature field at the time of the GPM overpass; and, IR brightness temperature field 30 minutes after the GPM overpass. The black horizontal line near 10 km in the A – B transect panels denote the approximate 235 – 240 Kelvin temperature level (approx. threshold for cloud shield distinction). The solid black circular line in all panels of the 1st, 3rd and 4th columns does not change, and is used for visually gauging the changing IR cloud shield size.

Supported by the results presented thus far, and building on the conceptual MCS sustainability ideas previously proposed (e.g., Yuter and Houze, 1998; Schumacher and Houze, 2007; Futyan and Del Genio, 2007), an analytical model of the system cloud shield time tendency, with source terms driven by a temporal generation-of-convective-area term, vertical convective and stratiform mass flux convergence terms forcing lateral cloud shield expansion, and a sink term proportional to the cloud area, can be structured as follows:

$$\frac{dA}{dt} \approx \frac{dA_c}{dt} - \frac{1}{\rho}\frac{dM_c}{dz} - \frac{1}{\rho}\frac{dM_s}{dz} - \frac{A}{\tau}, \tag{1}$$

where A is the cloud shield area, A_c is the convective area, M_c is the convective mass flux, M_s is the stratiform mass flux, ρ is the atmospheric density, and τ is a cloud shield area decay timescale. For comparison purposes, after moving the first term on the rhs of Eq. (1) to the lhs, the equation becomes one for the stratiform area time tendency, with the convective mass flux convergence term following Tiedtke (1993), Teixeira (2001) and follow-ons, and the decay term mimicking Hagos et al. (2020), although it is important to note that these terms were used in studies that were prognosing grid-box or fixed-domain stratiform *cloud fraction* or area changes whereas Eq. (1) prognoses *cloud physical area* changes following Lagrangian-tracked MCSs. Hagos et al. (2020) is further similar in that radar data (off the coast of Darwin, Australia) are used to develop a simple analytical model of stratiform area, though individual MCSs were not explicitly tracked in that analysis and the source terms vary in structure.

It is assumed that the time tendency of currently existing convective area A_c involves a transition to stratiform area, and a change in the cloud "type" does not result in a change in A. Since convective area being present is crucial for system growth and maintenance, as discussed, the time tendency of A_c is expected to be greater than or equal to zero *when averaged across all lifestages*, and representative of the mean regeneration of convective regions within a given system. A_c at any given time is estimated by GPM though the time tendency is not, owing to the long GPM orbit re-visit period. Therefore, this time tendency term is not well-constrained by current satellites.

Bony et al. (2016) and Seeley et al. (2019) explored the convective mass flux convergence term (equivalent to net detrainment) as it relates to understanding tropical cloud fraction sources. Using Weather Research and Forecasting (WRF) simulations, Seeley et al. (2019) found that net detrainment did not explain the altitude of peak cloud fraction. However, it is also evident in Seeley et al. (2019) that for cloud fraction profiles above ~10 km, where entrainment is minimal, convective source formulations represented as net or gross detrainment yield similar results. Such altitudes are closer to the IR-observed MCS cloud tops, and thus, a net detrainment formulation for the convective source term in our analysis is reasonable. The detrainment term can be re-cast in terms of Q_1-Q_R, allowing us to assess this formulation globally across the tropics using GPM Q_1-Q_R mapped to MCS shields. For any system, M_c is equivalent to $\rho A_c w$ (where w is the vertical wind speed averaged over A_c); but, M_c is not observable from GPM since vertical motion is not among those parameters retrieved. From the budget equation for dry static energy ($s = c_pT + gz$, where c_p is the specific heat at constant pressure, T is the temperature, and gz is the geopotential), if we assume small temporal changes in dry static energy across A_c, a small horizontal advection term, and assume convective Q_1-Q_R dominates over radiative heating within the convective cells, we can approximate w as follows:

$$w \approx \left(\frac{1}{c_p}\frac{ds}{dz}\right)^{-1}(Q_1\text{-}Q_{R_{\mathrm{Conv}}}) = \left(\frac{1}{\Gamma - \Gamma_d}\right)(Q_1\text{-}Q_{R_{\mathrm{Conv}}}), \tag{2}$$

where Γ is the average temperature lapse rate across A_c (and subscript d on Γ denotes the dry adiabatic lapse rate) and Q_1-Q_R is in units of K s^{-1}. A_c profiles are not provided by GPM (i.e., convective classification is independent of height) yet a spectrum of convective cells of varying vertical depths likely exists across A_c. Thus, as altitude increases and convective fraction systematically decreases (Kumar et al., 2015; Giangrande et al., 2016), w computed here might best be thought of as an approximate vertical motion across A_c that likely includes increasing contribution from non-convective motions above the tops of shallower or upward growing convective towers (as opposed to w representing convective core vertical updraft speeds at all altitudes, specifically). With Eq. (2), the second term on the rhs of Eq. (1) can now be approximated as follows:

$$-\frac{1}{\rho}\frac{dM_c}{dz} \approx -\frac{A_c}{\rho}\frac{d}{dz}\left(\rho\frac{Q_1\text{-}Q_{R_{\mathrm{Conv}}}}{\Gamma - \Gamma_d}\right). \tag{3}$$

The third term on the rhs of Eq. (1) can be written like Eq. (3), except with A_c and convective Q_1-Q_R being swapped for the stratiform counterparts. We include this third term in Eq. (1) since the mesoscale divergence near the tops of well-developed precipitating stratiform regions might be significant enough to force an observable lateral expansion of the entire cloud shield.

We use the satellite retrievals discussed in section 2 to populate the two source terms and plot both in Fig. 7. The satellite sounder retrievals of temperature are characteristic of non-cloudy unsaturated tropical environments outside of the tracked systems. Thus, to define Γ at all altitudes within any system cloud shield, we assume the atmosphere is saturated and assume a moist adiabatic lapse rate (hereafter, Γ_m) whose magnitude is set to the climatological AIRS grid box Γ_m closest to the tracked system. Since Γ_m varies strongly with temperature, this gives regionally varying lapse rates. As Fig. 7 shows, for both the CSH and SLH products, the convective source terms maximize ~1 – 2 km above the stratiform sources. Because of this, the stratiform source terms at lower altitudes would influence the vertical cloud extent and cloud area tendency profile below the cloud top. Thus, the downward-looking GEO-IR satellite perspective will yield a cloud shield tendency largely driven by the convective term, and we simplify Eq. (1) further by neglecting the stratiform source term. Fig. 7 suggests large differences in the vertical profiles of the cloud area tendencies derived from CSH and SLH. The altitude of the peak source is > 1 km higher in SLH than that inferred from the CSH product. For SLH, the convective and stratiform terms combined suggest a cloud fraction profile that would peak from 16 – 17 km, which is 1 – 2 km higher than observed (see Seeley et al., 2019). Therefore, we use the CSH heating product to quantify the magnitude of the convective source term, with the magnitude set to the profile maximum above 9 km (i.e., at or above the IR-identified altitude for cold "cloud shield" coverage).

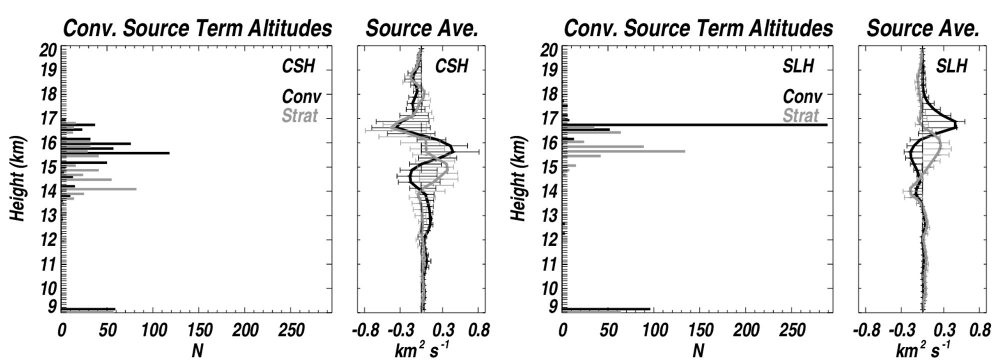

Figure 7. The left two panels show, for the CSH product, the height distribution of the maximum value of the cloud area tendency convective source term, and the composite-average source term profile (horizontal lines depict the +/– 1σ range). The right two panels: as in the left two panels, but for the SLH product.

Regarding the sink term of Eq. (1), dissipation of cloud area A depends on total ice condensate within cloud. GPM products do not provide all ice condensate species (not to mention the difficulty that exists in retrieving cloud ice accurately (Duncan and Eriksson, 2018)). Sources of ice include convective ice detrainment and saturated ascent in the stratiform/anvil region, with sinks being driven by precipitation. Convective and stratiform latent heating and precipitation terms could be used to partially infer ice condensate if the evolution of these terms along system paths were known; however, GPM provides these estimates at one instant, and though GPM estimates could constrain the current perturbation to total ice condensate within cloud, total ice condensate itself is not. Additionally, since evaporation is slow and inefficient in the cold upper troposphere (Seeley et al., 2019), mixing near cloud edges may actually act to increase cloud area if the ice condensate amount near cloud edges is large enough. These processes are all wrapped into the decay timescale τ of the Eq. (1) sink term. Given these unknowns (along with the unknown convective area regeneration term), and neglecting the stratiform source term following the previous discussion, we re-cast the cloud shield area time tendency equation as a regression equation with the terms formulated (and discretized) as follows:

$$\frac{\Delta A}{\Delta t} = \beta_0 - \beta_1 \frac{A_c}{\rho} \frac{\Delta}{\Delta z}\left(\rho \frac{Q_1\text{-}Q_{R_{\mathrm{Conv}}}}{\Gamma_m - \Gamma_d}\right) - \beta_2 A, \quad (4)$$

where $\Delta A/\Delta t$ is explicitly provided by TOOCAN ($\Delta t = 30$ min), β_0 is the convective area regeneration term, β_1 accounts for possible satellite retrieval limitations in quantifying the vertical profile of convective area and in-cloud lapse rates, and β_2 is equal to τ^{-1}.

3.3 Growth and Decay Rates stratified by surface type, system duration and convective organization

We apply Eq. (4) to data binned by convective system duration and A time tendencies. The A time tendency bin widths (~ 0.15 km^2 s^{-1}) are chosen so that compositing artifacts are minimized while ensuring each bin has at least one GPM sample. Results are coded (in Fig. 9) according to whether the system was over ocean (circles) or land (pluses) and colored according to how aggregated the convective cells were within the TOOCAN-tracked system shield. Cell aggregation is quantified by computing the ratio of the sum of convective perimeters to total convective area (referred to as R_{PA} hereafter). The sum of convective perimeters was computed by adding up all edge 4-km GPM DPR pixels surrounding the GPM identified convective regions of the tracked convective system. As R_{PA} increases, convection becomes dispersed, i.e., more cells for a given area (see Fig. 8 schematic for an illustration of systems with the same total cell area but different R_{PA}).

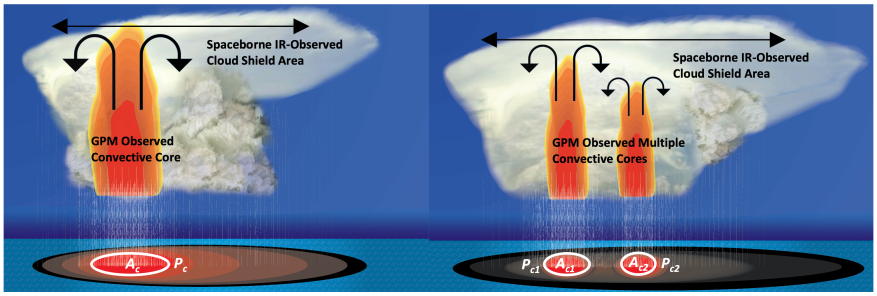

Figure 8. Schematic of distributed convective cores in tracked convective systems, where to the left, convection is aggregated into one cell of area A_c and cell perimeter P_c, and to the right, the same total convective area is observed, but is split across two convective cells of differing areas (A_{c1}, A_{c2}) and cell perimeters (P_{c1}, P_{c2}). Since $P_{c1} + P_{c2} > P_c$, the ratio of the sum of convective cell perimeters to total convective area (i.e., referred to as R_{PA} in the text) is larger for the system characterized by less aggregated convective area in the right panel.

Fig. 9 shows the predictions of the regression model vs. observed cloud shield area growth rates for storms of varying durations. The fact that most points fall close to the 1:1 line suggests that the functional form of the cloud shield model is skillful for both ocean and land across the spectrum of convective system duration bins and aggregation states. The regression β parameters are provided in each panel, and the cause of decreases in skill or outliers in some duration bins is discussed later. On average, β_0 ~ 0.5 km^2 s^{-1}. Over the IR 30-min time step, this implies a generation of new convective area equivalent to a circle of diameter ~ 30 km. β_1 varies little with system duration, with a median of ~1, suggesting that the mass flux convergence source term formulated in terms of diabatic heating and moist adiabatic lapse rates is a reasonable approximation. Relative to the other fit parameters, β_2 exhibits a slightly more systematic change across duration bins, with β_2 decreasing as system duration increases (~ 4e^{-4} for shorter-lived systems on average, to ~ 5e^{-5} for longer-lived systems). With β_2 having units of s^{-1}, this implies that the IR cloud shield decay timescale increases from ~ 0.75 hr for short-lived systems to 6 hr for longer-lived systems. Seeley et al. (2019) using model simulation experiments derived global ice cloud lifetimes of ~ 5 – 10 hr at 10 – 15 km, with a decrease in the lifetime as altitude increases further, while Hagos et al. (2020) derived a decay timescale of 7 hr for stratiform areas. The longer-lived systems with the largest cloud shields would contribute most to global anvil coverage. Therefore, the computed 6-hr timescale for the longer-duration system bins is probably most comparable to these other estimates, though the other decay timescales were computed for ensembles of convection as opposed to tracked systems, and thus the timescale are not apples-to-apples comparable. Considering the relative invariance in water vapor across systems (Fig. 5), we hypothesize that β_2 decreases (or decay timescale increases) as duration increases because longer-lived systems have more cloud shield ice condensate. Fig. 2 showed that longer-lived systems have larger Q_1-Q_R on average, and since this is predominantly a latent heating estimate, it is plausible that more condensate is generated as the longer-lived system moves through its lifecycle.

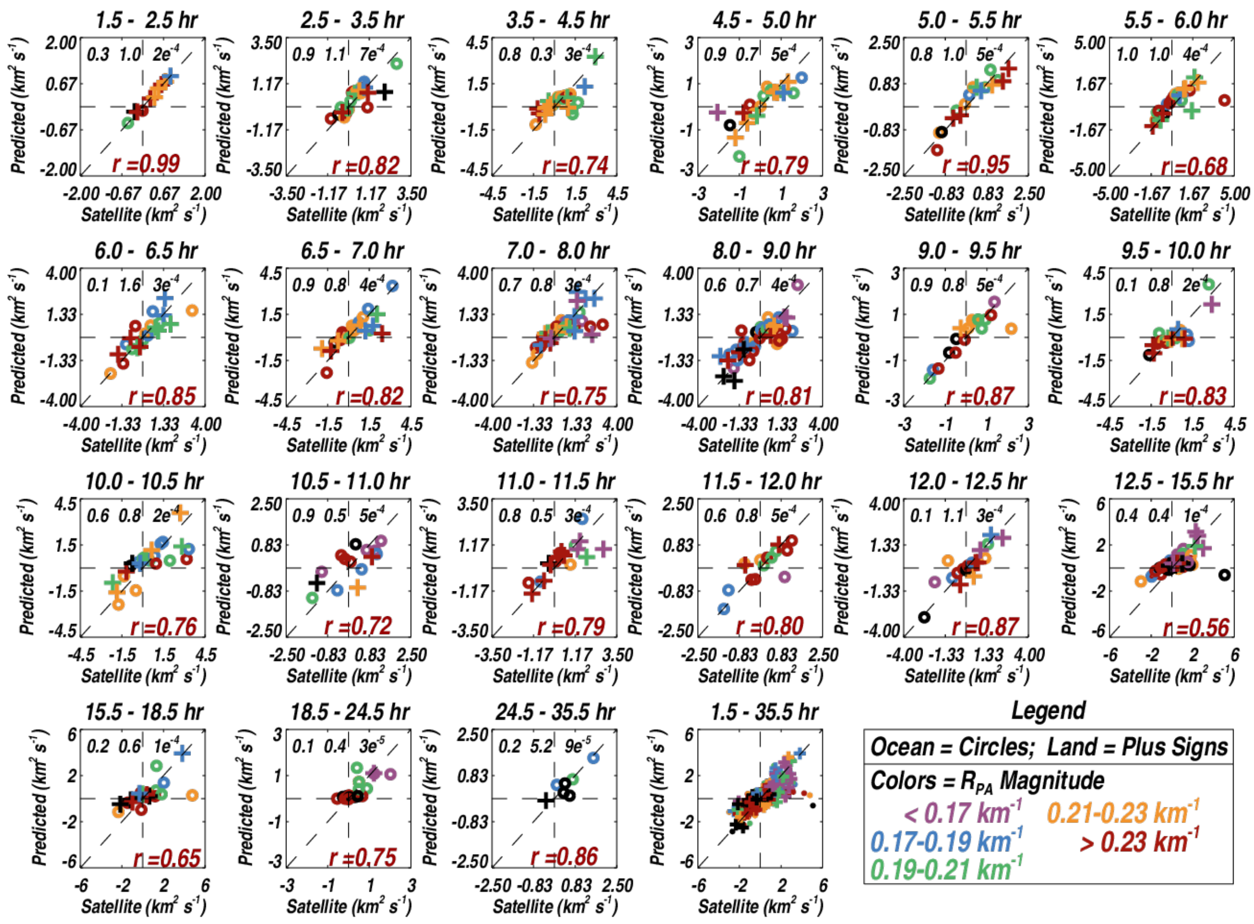

Figure 9. Predicted *dA/dt* versus satellite estimated *dA/dt* for different convective system duration bins, with the plot symbol denoting surface type (ocean = circles, land = plus signs) and symbol color denoting a convective aggregation metric (R_{PA} ; see text for description of metric). A black symbol color means GPM observed no convective cells at the time of overpass. Correlation coefficients are shown at the bottom of each panel, and Eq. (4) best fit constant and coefficients (β_0 [km^2 s^{-1}], β_1 [unitless], and β_2 [s^{-1}] respectively) are shown at the top of each panel. The last duration range panel shows all points combined for additional visual intercomparison.

Fig. 9 does not suggest a larger systematic deviation from the 1:1 line in the predictions for systems over land relative to those over ocean. As mentioned in section 3.1, convection is known to be more intense over land than ocean. The Eq. (2) formulation for the convective source term yields a source magnitude that peaks near 16.5 km over land and 15.5 km over ocean, with the source itself a factor of ~2.5 stronger over land than ocean on average (0.8 km^2 s^{-1} and 2.0 km^2 s^{-1} for ocean and land, respectively). These results are consistent with land – ocean differences in convection, with the increased land source attributed to stronger diabatic heating and a larger vertical gradient in diabatic heating instead of being attributed to moist adiabatic lapse rate differences (not shown). Additionally, departures in the prediction from the 1:1 line do not seem to be dependent on cell aggregation (i.e., R_{PA}). This result is interesting, particularly in light of Hagos et al. (2020) where it was found that if there were more convective cells for a given convective area, growth of the stratiform area was larger. The Hagos et al. (2020) result was interpreted within the context of the "particle fountain" idea proposed by Yuter and Houze (1995), where if convective cells were more scattered like trees in a forest, their ice particles were more likely to fall outside of the existing convective area, thus favoring growth of stratiform cloud regions. For a given convective area, as the number of convective cells increases, the sum of the perimeters surrounding convective cells increases (Fig. 8); therefore, growth of the stratiform region (or cloud shield area in this study, given the correlation with stratiform area) should be larger as R_{PA} increases. Since the source – sink model does not specifically consider convective perimeters, the lack of outliers in the prediction might be surprising.

We investigate this further in Fig. 10, where the convective source term (i.e., Eq. 3) is plotted as a joint function of convective area A_c and $R_{PA.}$ R_{PA} is one way to quantify convective aggregation, but this metric is also strongly correlated with an independent convective "organization" metric (i.e., the Radar Organization Metric or ROME; plotted in bottom right of Fig. 10) following Retsch et al. (2020) which specifically defines organization based on the size and proximity of convective cells. As defined here, organization increases as ROME increases, with the upper limit of organization being equivalent to the mean convective cell area multiplied by 2. The bottom left panel of Fig. 10 shows how ROME increases as R_{PA} decreases for the same convective area. As expected, Fig. 10 shows that the convective source term increases as A_c increases (and, indeed, the total satellite cloud shield time tendency in the upper right panel of Fig. 10 follows this pattern). Additionally, there is a very clear pattern showing an increase in the convective source term as R_{pa} decreases. Interestingly, this tendency reverses when the cloud shield area is undergoing decay on average. In this state, as R_{pa} increases (i.e., organization decreases), the source term also increases. The latter result is similar to the findings of Hagos et al. (2020). Might this imply that less organized convection during the later decaying stages of system lifecycles favors cloud shield sustenance and increased longevity? At first glance, this seems to be a small portion of the data state space; however, this region of the state space comprises large cloud shield areas and system counts (roughly 20-25% of the data lie above the white-outlined area in the top left panel of Fig. 10). In summary, even though Eq. (4) does not specifically consider convective cell aggregation, there is a signal in the vertical (associated with the convective cell-ensemble Q_1-Q_R height derivative) that is serving as a strong enough proxy to modulate variations in the cloud area source as convective cell organization changes, which is probably why Fig. 9 shows no clear biases in the prediction as cell aggregation varies.

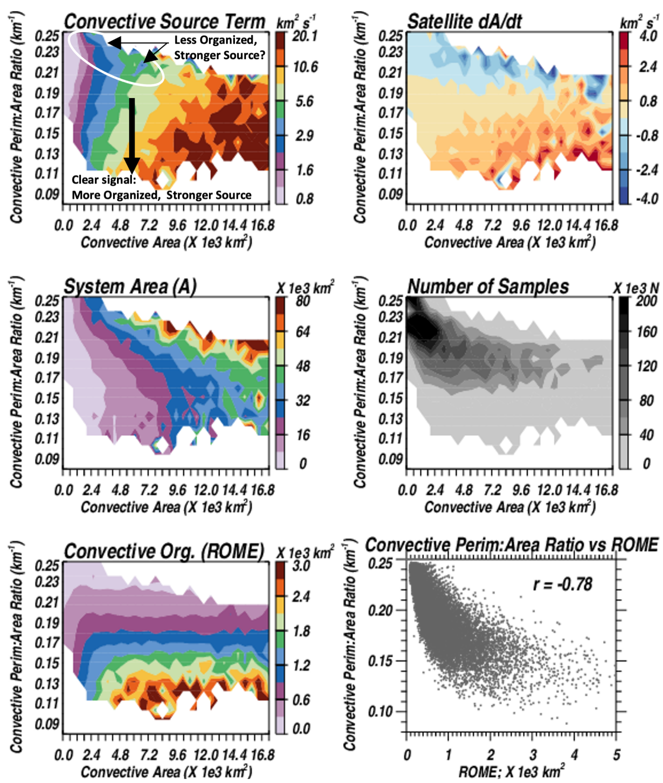

Figure 10. (Left column) From top to bottom, the average convective source term (Eq. 3 in manuscript), average convective system IR-estimated cloud shield area, and average organization of convective cells (defined using the Radar Organization Metric, or ROME, as in Retsch et al. 2020) as a joint function of total convective area (A_c) and the ratio of the sum of convective cell perimeters divided by total convective area (R_{PA}). (Right column) As in left, for first two panels: satellite estimated system area time tendency (*dA/dt*) and number of samples contributing to composites. The bottom right panel illustrates the relationship between R_{PA} and ROME.

3.4 Sensitivity of Source – Sink Model to Areal Coverage Thresholds and Convective Q_1-Q_R

There are some duration bins (e.g., 5.5 – 6.0, 12.5 – 15.5, 15.5 – 18.5 hr) exhibiting systematic lower sensitivity of the prediction relative to observations (characterized by larger predicted minus satellite cloud shield area differences, more outliers and/or smaller duration bin correlations). Over 90% of the time when the predicted minus satellite estimated differences exceed 1 $km^2\ s^{-1}$, the MCS cloud shield area was under-sampled by GPM. As mentioned in section 2.1, at least 2/3 of the convective system cloud shield area must be sampled by GPM in order for the data point to be included in development and analysis of the analytical model. Convection occupies a small fraction of a cloud shield, and therefore, it is easy for GPM to completely miss convective cores. This limitation is not resolved by simply increasing the size of our database. Instead, this is the result of system sizes often exceeding the swath width of the GPM DPR orbit, and no sample size will ever permit 2/3 sampling of large MCS shields (Nesbitt et al., 2006; Fiolleau and Roca, 2013b).

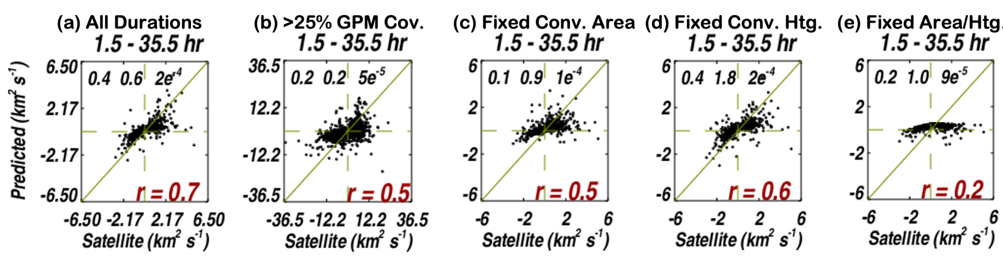

Figure 11. Similar to Fig. 9, except with varying thresholds used for constraining the convective source term in the cloud shield area time tendency equation and no coding of points based on surface type (land, ocean) or convective organization. From L to R: (a) fits calculated independent of duration bin; (b) calculations performed with less stringent GPM coverage required (>25% of the system shield must be sampled); (c) calculations performed while fixing the convective area to the average across all systems; (d) calculations performed while fixing the convective heating profile to the average across all systems; and, (e) calculations performed while fixing both convective area and convective heating profiles to the average across all systems.

While decreasing the 2/3 coverage threshold drastically increases the sample count, there is a price to pay. If convection is missed too often, the cloud source term is artificially zero too frequently. This issue does not simply lead to more scatter in any one duration bin. Instead, with a weaker (or zero) source term, a weaker sink term would also be computed to achieve the best fit to the ensemble of points, and subsequently, the sensitivity of the prediction is lower. We suspect this might be happening in a few of the aforementioned bins, depicted as a "flattening" in the prediction. Conversely, a more conservative threshold (e.g. 90% coverage), while increasing the probability that convective cores are sampled, results in almost no data being available no matter the record length (and for systems that are sampled, their sizes are often small, since smaller shields are the ones entirely viewable by GPM). Thus, the 2/3 threshold strikes a balance between data samples and system sizes, and the necessity of sampling the convective source. To assess the under-sampling issue further, one fit is re-computed independent of duration bin (Fig. 11a), and another fit is recomputed after requiring only 25% of the area to be covered by GPM (Fig. 11b). Clearly, the relationship is not as strong with less sampling of the convective structures, and both growth and decay rates are further underestimated.

Is the vertical convective heating structure or convective area the key component driving the convective source term role? As a test for system convective core similarity, we swap the mean convective area across all systems for the actual observed convective area and re-compute the fit, and a weakened relationship is noted (Fig. 11c). In Fig. 11d, the all-systems-average convective profile is substituted in, and Fig. 11e shows the results when there is no variation in convection across systems (i.e., mean convective area and mean profile are used). Clearly, capturing both the convective area and heating profile via sampling of a large-enough fraction of the system is important, and substitution of a "characteristic" unvarying, average convective heating profile and convective area size leads to poorer fits.

4 Conclusion

How tropical anvil areal extent will change and modulate radiation as the climate warms is one of the largest uncertainties in recent cloud feedback assessments (e.g., Sherwood et al., 2020), and improved understanding of the spectrum of deep convective system areal extents, how system areas couple with convective and stratiform diabatic heating, and the construction of simple models that can inform GCM convective parameterization is needed. In this work, we specifically focused on increasing our understanding of MCS cloud shield area time tendencies and relationship with convective heating.

Composite analyses show that longer-lived (and larger) deep convective system cloud shields are associated with increased diabatic heating above the melting level (Fig. 2), largely due to stratiform region heating. The composite results are similar for systems over land and ocean, suggesting that ocean-land differences and regional climatological composites may best be considered an emergent property arising from differences in occurrence frequencies of varying-duration (and hence, size) systems whose composite evolutions themselves are self-similar if stratified by duration. The system evolution composites are not necessarily representative of individual system evolutions, though (e.g., Fig. 4). Instead, evolutions may be best thought of as collections of instantaneous bursts in growth mixed with sequences of decay, such that a longer-lived duration may arise from a fortunate series of growth sequences. Results suggest that the growth of a convective system shield is strongly related to generation of convective area and a strong vertical gradient of convective-region heating (computed from its peak above the melting level to the cloud top) forcing lateral cloud growth (Fig. 5). Decay rates are strongly related to the instantaneous size of the cloud shield itself, but exhibit no clear dependence on relative humidity.

A simple convective-source, slow-decay model (Eqs. 1 and 4) informed by the observational results is developed. Since satellite-estimated vertical winds in convection are not available for developing the cloud shield model source term, the model is re-formulated in terms of diabatic heating, an advantage that permits analyses via use of GPM retrieved diabatic heating mapped to MCSs (and which has an analog in GCM output since most convective parameterizations yield diabatic heating profiles). The remaining model terms are quantified using satellite retrievals from GEO-IR, AIRS/MLS and convective area estimates from GPM, and uncertain or unknown coefficients are derived by applying the model to all tropical (land and ocean) scenes and duration bins. The simple cloud shield model often explains well over 50% of the 30-min changes in cloud shield areas across the global tropics (with comparable skill across MCS duration bins, and no clear biases for land or ocean systems nor convective cell aggregation). There is a rich structure in the cloud area source term that varies as a function of convective cell organization, with overall, the source term increasing with convective organization, while for decaying shields characterized by smaller convective area overall, the source term sometimes increases as organization decreases. Results further suggest that convective and stratiform rainfall and associated diabatic heating are often coupled, stratiform heating is present at all system lifecycle stages past initiation (Fig. 3), and stratiform area is continually produced along the path of the MCS (Eq. 1). Thus, the "convective to stratiform transition" onset period might also be considered an emergent property, useful for evaluating output from a GCM at the grid box and timestep-scales during parameterization development, as opposed to a process that happens abruptly or at a fixed lifecycle stage.

Toward understanding the distribution of convective system durations, work is underway to understand factors favoring convective area maintenance and/or re-generation following the path of a system. Extending the Lagrangian analyses to three-dimensional MCS cloud volumes via analyses of height-resolved cloud fractions alongside the stratiform area source term, exploring the role of radiative heating (Gasparini et al., 2019) in cloud shield time tendencies, and understanding how precipitation sinks and organization metrics impact the cloud shield decay term are other avenues worth pursuing. An overall objective is to provide improved process-level understanding and useful observational depictions for improving the representation of convection in parameterized GCMs tasked with providing projections of 21st century climate, the reliability of which depends on accurately representing the spectrum of cloud feedbacks (Hartmann and Larson, 2002; Zelinka and Hartmann, 2010, 2011; Bony et al., 2015), including the role of organized convection (Moncrieff, 2019) and convection-driven high cloudiness.

Acknowledgements

Computing resources for data analysis were provided by the NASA High-End Computing (HEC) Program through the NASA Center for Climate Simulation (NCCS) at the Goddard Space Flight Center. This research was supported by the Precipitation Measurement Missions program (RTOP WBS #573945.04.18.03.60), the Terra, Aqua, and Suomi NPP program (Grant #80NSSC18K1030), and the NASA Data for Operation and Assessment program (Grant #NNX17AF46G). All data used for analysis and analytical model development are available in the public domain. The TOOCAN convective system tracking database is available at https://toocan.ipsl.fr/toocandatabase/. The GPM CSH and SLH Q_1-Q_R, rainfall and convective-stratiform pixel identification are available from NASA's Goddard Earth Sciences Data and Information Services Center (GES DISC) at https://gpm1.gesdisc.eosdis.nasa.gov/data/GPM_L2/, while AIRS V6 water vapor Level 2 data mapped to MCSs are available from GES DISC at https://disc.gsfc.nasa.gov/datasets/AIRS2RET_006/summary/. AIRS V6 and MLS V3 gridded (Level 3) datasets used for computation of climatological moist adiabatic lapse rates are available from the Observations for Model Intercomparison Project (Obs4MIPS) archive hosted on the Earth System Grid Federation at https://esgf-node.llnl.gov/projects/obs4mips/SatelliteDataProducts.

Helpful comments by external referees provided on an earlier manuscript submitted for review are acknowledged.

REFERENCES

Bony, S., B. Stevens, D.M.W. Frierson, C. Jakob, M. Kageyama, R. Pincus, T.G. Shepherd, S.C. Sherwood, A.P. Siebesma, A.H. Sobel, M. Watanabe, and M.J. Webb, 2015: Clouds, circulation and climate sensitivity. *Nature Geosci.,* **8**, 261-268.

Bony, S., B. Stevens, D. Coppin, T. Becker, K.A. Reed, A. Voigt, and B. Medeiros, 2016: Thermodynamic control of anvil cloud amount. *Proc. Nat. Acad. Sci.,* **113**, 8927-8932.

Bouniol, D., R. Roca, T. Fiolleau, and D. E. Poan, 2016: Macrophysical, Microphysical, and Radiative Properties of Tropical Mesoscale Convective Systems over Their Life Cycle. *J. Clim.*, **29**, 3353–3371.

Chahine, M. T., et al., 2006: AIRS: Improving weather forecasting and providing new data on greenhouse gases. *Bull. Amer. Meteor. Soc.*, **87**, 911–926.

Duncan, D.I., C.D. Kummerow, and G.S. Elsaesser, 2014: A Lagrangian analysis of deep convective systems and their local environmental effects. *J. Clim.*, **27**, 2072-2086.

Duncan, D.I., and P. Eriksson, 2018: An update on global atmospheric ice estimates from satellite observations and reanalyses. *Atmos. Chem. Phys.*, **18**, 11205-11219.

Elsaesser, G.S., C.D. Kummerow, T.S. L'Ecuyer, Y.N. Takayabu, and S. Shige, 2010: Observed self-similarity of precipitation regimes over the tropical oceans. *J. Clim.*, **23**, 2686-2698.

Elsaesser, G.S., and C.D. Kummerow, 2013: A multisensor observational depiction of the transition from light to heavy rainfall on subdaily time scales. *J. Atmos. Sci.,* **70**, 2309-2324.

Elsaesser, G.S., A.D. Del Genio, J. Jiang, and M. van Lier-Walqui, 2017: An improved convective ice parameterization for the NASA GISS Global Climate Model and impacts on cloud ice simulation. *J. Clim.*, **30**, 317-336.

Feng, Z., X. Dong, B. Xi, S. A. McFarlane, A. Kennedy, B. Lin, and P. Minnis, 2012: Life cycle of midlatitude deep convective systems in a Lagrangian framework, *J. Geophys. Res.*, **117**, D23201, doi:10.1029/2012JD018362.

Feng, Z., L. R. Leung, R. A. Houze, S. Hagos, J. Hardin, Q. Yang, Q., et al., 2018: Structure and evolution of mesoscale convective systems: Sensitivity to cloud microphysics in convection-permitting simulations over the United States. *JAMES*, **10**, 1470–1494.

Feng, Z., R. A. Houze, L. R. Leung, F. Song, J. C. Hardin, J. Wang, W. I. Gustafson, and C. R. Homeyer, 2019: Spatiotemporal Characteristics and Large-Scale Environments of Mesoscale Convective Systems East of the Rocky Mountains. *J. Clim.*, **32**, 7303–7328.

Feng, Z., F. Song, K. Sakaguchi, and L. R. Leung, 2020: Evaluation of Mesoscale Convective Systems in Climate Simulations: Methodological Development and Results from MPAS-CAM over the U.S. *J. Clim.*, **in press**.

Fiolleau, T., and R. Roca, 2013a: An algorithm for the detection and tracking of tropical mesoscale convective systems using infrared images from geostationary satellite. *IEEE Trans. Geosci. Remote Sens.,* **51**, 4302-4315.

Fiolleau, T., and R. Roca, 2013b: Composite life cycle of tropical mesoscale convective systems from geostationary and low Earth orbit satellite observations: method and sampling considerations. *Q. J. R. Meteorol. Soc.,* **139**, 941-953.

Fiolleau, T., R. Roca, S. Cloché, D. Bouniol, P. Raberanto, 2020: Homogenization of geostationary infrared imager channels for cold cloud studies using Megha-Tropiques/ScaRaB. *IEEE Trans. Geosci. Remote Sens.*, **58**, 6609-6622.

Futyan, J., and A. D. Del Genio, 2007: Deep convective system evolution over Africa and the tropical Atlantic. *J. Clim.*, **20**, 5041-5060.

Gasparini B., P. N. Blossey, D. L. Hartmann, G. Lin, and J. Fan, 2019: What drives the life cycle of tropical anvil clouds? *JAMES*, **11**, 2586–2605. https://doi. org/10.1029/2019MS001736.

Giangrande, S. E., T. Toto, M. P. Jensen, M. J. Bartholomew, Z. Feng, A. Protat, C. R. Williams, C. Schumacher, and L. Machado, 2016: Convective cloud vertical velocity and mass-flux characteristics from radar wind profiler observations during GoAmazon2014/5. *J. Geophys. Res. Atmos.*, **121**, 12891–12913.

Grecu, M., W.S. Olson, S.J. Munchak, S. Ringerud, L.Liao, Z.S. Haddad, B.L. Kelley, and S.F. McLaughlin, 2016: The GPM combined algorithm. *J. Atmos. Ocean. Tech.,* **33**, 2225-2245.

Hagos, S., Z. Feng, S. McFarlane, and L. R. Leung, 2013: Environment and the Lifetime of Tropical Deep Convection in a Cloud-Permitting Regional Model Simulation. *J. Atmos. Sci.*, **70**, 2409–2425.

Hagos, S., Z. Feng, R. S. Plant, and A. Protat, 2020: A machine learning assisted development of a model for the populations of convective and stratiform clouds. *JAMES*, **12**, doi: 10.1029/2019MS001798.

Hannah, W.M., B.E. Mapes, and G.S. Elsaesser, 2016: A Lagrangian view of moisture dynamics during DYNAMO. *J. Atmos. Sci.*, **73**, 1967-1985.

Hartmann, D.L., H.H. Hendon, and R.A. Houze Jr., 1984: Some implications of the mesoscale circulations in tropical cloud clusters for large-scale dynamics and climate. *J. Atmos. Sci.,* **41**, 113-121.

Hartmann, D.L., and K. Larson, 2002: An important constraint on tropical cloud-climate feedback. *Geophys. Res. Letters,* **29**, 1951, doi:10.1029/2002GL015835.

Holloway, C.E., A.A. Wing, S. Bony, C. Muller, H. Masunaga, T.S. L'Ecuyer, D.D. Turner, and P. Zuidema, 2017: Observing convective aggregation. *Surv. Geophys.,* **38**, 1199-1236.

Houze, R. A. Jr., 1989: Observed structure of mesoscale convective systems and implications for large scale heating. *Quart. J. R. Meteor. Soc.*, **115**, 425– 461.

Houze, R. A. Jr., 1997: Stratiform Precipitation in Regions of Convection: A Meteorological Paradox? *Bull. Amer. Meteor. Soc.*, **78**, 2179–2196.

Houze, R. A., 2004: Mesoscale convective systems. *Rev. Geophys*. **42**, 1–43.

Iguchi, T., S. Seto, et al., 2012: An overview of the precipitation retrieval algorithm for the Dual-frequency Precipitation Radar (DPR) on the Global Precipitation Measurement (GPM) mission's core satellite. https://doi.org/10.1117/12.976823.

Inoue, K., and L. Back, 2015: Column-Integrated Moist Static Energy Budget Analysis on Various Time Scales during TOGA COARE, *J. Atmos. Sci*, **72**, 1856-1871.

Knapp, K. R., M. C. Kruk, D. H. Levinson, H. J. Diamond, and C. J. Neumann, 2010: The International Best Track Archive for Climate Stewardship (IBTrACS), *Bull. Amer. Meteor. Soc.*, **91**(3), 363-376.

Kumar, V. V., C. Jakob, A. Protat, C. R. Williams, and P. T. May, 2015: Mass-Flux Characteristics of Tropical Cumulus Clouds from Wind Profiler Observations at Darwin, Australia. *J. Atmos. Sci.*, **72**, 1837–1855.

Lang, S.E., and W.-K. Tao, 2018: The next-generation Goddard Convective-Stratiform Heating algorithm: New tropical and warm season retrievals for GPM. *J. Clim.*, **31**, 5997-6026.

Lin, L., Q. Fu, X. Liu, Y. Shan, S.E. Giangrande, G.S. Elsaesser, K. Yang, and D. Wang, 2021: Improved convective ice microphysics parameterization in the NCAR CAM model. *J. Geophys. Res. Atmos.*, **126**, no. 9, e2020JD034157, doi:10.1029/2020JD034157.

Liu, C., E. J. Zipser, D. J. Cecil, S. W. Nesbitt, and S. Sherwood, 2008: A Cloud and Precipitation Feature Database from Nine Years of TRMM Observations. *J. Appl. Meteor. Clim.*, **47**, 2712-2728.

Liu, C., 2011: Rainfall Contributions from Precipitation Systems with Different Sizes, Convective Intensities, and Durations over the Tropics and Subtropics, *J. Hydrometeor.*, **12**, 394-412.

Liu, C., S. Shige, Y. N. Takayabu, and E. Zipser, 2015: Latent Heating Contribution from Precipitation Systems with Different Sizes, Depths, and Intensities in the Tropics, *J. Clim.,* **28**, 186-203.

Lucas, C., E. J. Zipser, and M. A. Lemone, 1994: Vertical velocity in oceanic convection off tropical Australia. *J. Atmos. Sci.*, **51(21)**, 3183-3193.

Machado, L.A.T., W.B. Rossow, R.L. Guedes, and A.W. Walker, 1998: Life cycle variations of mesoscale convective systems over the Americas. *Mon. Wea. Rev.*, **126**, 1630-1654.

Machado, L.A.T, and H. Laurent, 2004: The convective system area expansion over Amazonia and its relationship with convective system life duration and high-level wind divergence. *Mon. Wea. Rev.*, **132**, 714–725.

Mapes, B., and R. Neale, 2011: Parameterizing convective organization to escape the entrainment dilemma. *JAMES*, **3**, M06004, doi:10.1029/2011MS000042.

Mauritsen, T., and Coauthors, 2012: Tuning the climate of a global model. *J. Adv. Model. Earth Syst.*, **4**, M00A01, doi:10.1029/2012MS000154.

Moncrieff, M.W., C. Liu, and P. Bogenschutz, 2017: Simulation, modeling, and dynamically based parameterization of organized tropical convection for global climate models. *J. Atmos. Sci.*, **74**, 1363-1380.

Moncrieff, M. W., 2019: Toward a Dynamical Foundation for Organized Convection Parameterization in GCMs. *Geophys. Res. Lett.*, **46**, 14103– 14108.

Naud, C.M., A.D. Del Genio, M. Bauer, and W. Kovari, 2010: Cloud vertical distribution across warm and cold fronts in CloudSat-CALIPSO data and a general circulation model. *J. Clim.*, **23**, 3397-3415.

Naud, C. M., J. F. Booth, J. F., and A. D. Del Genio, 2016: The Relationship between Boundary Layer Stability and Cloud Cover in the Post-Cold-Frontal Region, *J. Clim.*, **29**, 8129-8149.

Nesbitt, S. W., R. Cifelli, and S. A. Rutledge, 2006: Storm Morphology and Rainfall Characteristics of TRMM Precipitation Features. *Mon. Weather Rev.*, **134**, 2702–2721.

Parker, M. D., and R. H. Johnson, 2000: Organizational Modes of Midlatitude Mesoscale Convective Systems. *Mon. Wea. Rev.*, **128**, 3413–3436.

Prein, A. F., C. Liu, K. Ikeda, S. B. Tier, R. M. Rasmussen,, G. J. Holland, and M. P. Clark, 2017: Increased rainfall volume from future convective storms in the US. *Nat. Clim. Chang.*, **7**, 880–884.

Rapp, A.D., G. Elsaesser, and C. Kummerow, 2009: A combined multisensor optimal estimation retrieval algorithm for oceanic warm rain clouds. *J. Appl. Meteorol. Climatol.*, **48**, 2242-2256.

Retsch, M. H., C. Jakob, and M. S. Singh, 2020: Assessing Convective Organization in Tropical Radar Observations. *J. Geophys. Res.: Atmos.*, **125**, e2019D031801.

Roca, R., J. Aublanc, P. Chambon, T. Fiolleau, and N. Viltard, 2014: Robust Observational Quantification of the Contribution of Mesoscale Convective Systems to Rainfall in the Tropics. *J. Clim.*, **27**, 4952–4958.

Roca, R., T. Fiolleau, and D. Bouniol, 2017: A simple model of the life cycle of mesoscale convective system cloud shield in the tropics. *J. Clim.,* **30**, 4283-4298.

Roca, R., and T. Fiolleau, 2020: Extreme precipitation in the tropics is closely associated with long-lived convective systems. *Commun. Earth. Environ.* **1,** 18.

https://doi.org/10.1038/s43247-020-00015-4.

Schiro, K. A., S. C. Sullivan, Y.-H. Kuo, H. Su, P. Gentine, G. S. Elsaesser, J. H. Jiang, J. D. Neelin, 2020: Environmental controls on tropical mesoscale convective system precipitation intensity. *J. Atmos. Sci.,* **in press**, doi:10.1175/JAS-D-200111.1.

Schmidt, G.A., D. Bader, L.J. Donner, G.S. Elsaesser, J.-C. Golaz, C. Hannay, A. Molod, R. Neale, and S. Saha, 2017: Practice and philosophy of climate model tuning across six U.S. modeling centers. *Geosci. Model Dev.*, **10**, 3207-3223, doi:10.5194/gmd-10-3207-2017.

Schneider, T., S. Lan, A. Stewart, and J. Teixeira, 2017: Earth system modeling 2.0: A blueprint for models that learn from observations and targeted high-resolution simulations. *Geophys. Res. Lett.,* **44**, 12396-12417.

Schumacher, C. and R. A. Houze Jr., 2003a: Stratiform rain in the tropics as seen by the TRMM Precipitation Radar. *J. Clim.,* **116**, 1739-1756.

Schumacher, C. and R. A. Houze Jr., 2003b: The TRMM Precipitation Radar's view of shallow, isolated rain. *J. Appl. Meteorol.,* **42**, 1519-1524.

Schumacher, C., R.A. Houze Jr., and I. Kraucunas, 2004: The tropical dynamical response to latent heating estimates derived from the TRMM Precipitation Radar. *J. Atmos. Sci.,* **61**, 1341-1358.

Schumacher, C. and R. A. Houze Jr., 2006: Stratiform precipitation production over sub-Saharan Africa and the tropical East Atlantic as observed by TRMM. *Q.J.R. Meteorol. Soc.,* **132**, 2235-2255.

Seeley, J. T., N. Jeevanjee, W. Langhans, and D. M. Romps, 2019: Formation of tropical anvil clouds by slow evaporation. *Geophys. Res. Lett.*, **46**, https://doi.org/10.1029/2018GL080747.

Sherwood, S. C., M. J. Webb, J. D. Annan, J. D., K. C. Armour, P. M. Forster, J. C. Hargreaves, et al., 2020: An assessment of Earth's climate sensitivity using multiple lines of evidence. *Reviews of Geophysics*, 58, e2019RG000678.

Shige, S., Y.N. Takayabu, S. Kida, W.-K. Tao, X. Zeng, C. Yokoyama, and T. L'Ecuyer, 2009: Spectral retrieval of latent heating profiles from TRMM PR data. Part IV: Comparisons of lookup tables from two- and three-dimensional simulations. *J. Clim.*, **22**, 5577-5594.

Skofronick-Jackson, et al., 2017: The Global Precipitation Measurement (GPM) Mission for Science and Society, *Bull. Amer. Meteor. Soc.*, **98**, 1679-1695.

Takahashi, H., Z. J. Luo, and G. L. Stephens, 2017: Level of neutral buoyancy, deep convective outflow, and convective core: New perspectives based on 5 years of CloudSat data. *J. Geophys. Res.: Atmos.*, **122(5)**, 2958-2969.

Takahashi, H., Z. J. Luo, and G. L. Stephens, 2021: Revisiting the entrainment relationship of convective plumes: A perspective from global observations, *Geophys. Res. Lett.*, https://doi.org/10.1029/2020GL092349.

Tan, J., C. Jakob, W.B. Rossow, and G. Tselioudis, 2015: Increases in tropical rainfall driven by changes in frequency of organized deep convection. *Nature,* **519**, 451-454.

Tao, W.-K., and M. W. Moncrieff, 2009: Multiscale cloud system modeling. *Rev. Geophys.*, 47, RG4002, doi:10.1029/2008RG000276.

Teixeira, J., 2001: Cloud Fraction and Relative Humidity in a Prognostic Cloud Fraction Scheme. *Mon. Wea. Rev.*, **129**, 1750–1753.

Tiedtke, M., 1993: Representation of Clouds in Large-Scale Models. *Mon. Wea. Rev.,* **121**, 3040 - 3061.

Tobin, I., S. Bony, and R. Roca, 2012: Observational evidence for relationships between the degree of aggregation of deep convection, water vapor, surface fluxes, and radiation. *J. Climate,* **25**, 6885-6904.

Tobin, I., S. Bony, C.E. Holloway, J.Y. Grandpeix, G. Seze, D. Coppin, S.J. Woolnough, and R. Roca, 2013: Does convective aggregation need to be represented in cumulus parameterizations? *JAMES,* **5**, 692-703.

Vant-Hull, B., W. Rossow, and C. Pearl, 2016: Global comparisons of regional life cycle properties and motion of multiday convective systems: tropical and midlatitude land and ocean. J. *Clim*. **29**, 5837–5858.

Wang, D., S. E. Giangrande, K. Schiro, M. P. Jensen, and R. A. Houze, 2019: The characteristics of tropical and midlatitude mesoscale convective systems as revealed by radar wind profilers. *J. Geophys. Res. Atmos.*, **124**, 4601– 4619.

Wang, D., S. E. Giangrande, Z. Feng, J. C. Hardin, and A. F. Prein, 2020: Updraft and downdraft core size and intensity as revealed by radar wind profilers: MCS observations and idealized model comparisons. *J. Geophys. Res. Atmos.*, **125**, https://doi.org/10.1029/2019JD031774.

Waters, J. W., et al., 2006: The Earth Observing System Microwave Limb Sounder (EOS MLS) on the Aura Satellite. *IEEE Trans. Geosci. Rem. Sens.*, **44**, 1075-1092.

Yuter, S. E., and R. A. Houze Jr., 1995: Three-dimensional kinematic and microphysical evolution of Florida cumulonimbus. Part III: Vertical mass transport, mass divergence, and synthesis. *Mon. Wea. Rev.,* **123**, 1964-1983.

Yuter, S. E., and R. A. Houze Jr., 1998: The natural variability of precipitating clouds over the western Pacific warm pool. *Q. J. R. Meteorol. Soc.,* **124**, 53-99.

Zelinka, M.D., and D.L. Hartmann, 2010: Why is longwave cloud feedback positive? *J. Geophys. Res.,* **115**, D16117, doi:10.1029/2010JD013817.

Zelinka, M.D., and D.L. Hartmann, 2011: The observed sensitivity of high clouds to mean surface temperature anomalies in the tropics. *J. Geophys. Res.,* **116**, D23103, doi:10.1029/2011JD016549.

Zipser, E. J., and M. A. LeMone, 1980: Cumulonimbus vertical velocity events in GATE. Part II: Synthesis and model core structure. *J. Atmos. Sci.*, **37(11)**, 2458-2469.